Angular dependence of the magnetization relaxation in Co/Pt multilayers

OPEN ACCESS
IOP Publishing
Journal of Physics: Condensed Matter
J. Phys.: Condens. Matter **36** (2024) 015802 (7pp)
https://doi.org/10.1088/1361-648X/acfc8f

Angular dependence of the magnetization relaxation in Co/Pt multilayers

Anil Adhikari[1], Bryce Herrington[1], Nhat Nguyen[1], Ruthi Zielinski[1], Ather Mahmood[1], Shireen Adenwalla[1,2] and Robert Streubel[1,2,*]

[1] Department of Physics and Astronomy, University of Nebraska-Lincoln, Lincoln, NE 68588, United States of America
[2] Nebraska Center for Materials and Nanoscience, University of Nebraska-Lincoln, Lincoln, NE 68588, United States of America

E-mail: streubel@unl.edu

Received 21 March 2023, revised 19 June 2023
Accepted for publication 22 September 2023
Published 29 September 2023

Abstract

We study the influence of defects in Co/Pt multilayers on the room-temperature magnetization reversal and relaxation mechanisms via angle-dependent magnetic viscosity and coercive field measurements. The data reveal a transition from pinning-dominated domain wall propagation to a sequence of pinning-dominated and uniform switching, with increasing tilt away from the normal direction. The leading role of the dendritic domain wall propagation in the nanogranular exchange-coupled films is corroborated by the scaling of relaxation times, the angular dependence of the coercive field, and Kerr microscopy.

Keywords: magnetization relaxation, perpendicular magnetic anisotropy, magnetometry

1. Introduction

Relaxation is a thermally activated Arrhenius-type phenomenon of domain growth (or creep) in the presence of activation barriers that has been observed in disparate materials over a wide range of timescales. The temporal evolution is governed by the activation energy distribution, which is difficult (or impossible) to quantify experimentally. Structural, thermodynamic, mechanical, and magnetic relaxation measurements show a surprising uniformity following $\exp[-\left(\frac{t}{\tau}\right)^{\beta}]$ with the characteristic relaxation time τ and the exponent β governed by the activation barrier distribution via the Arrhenius–Néel law [1] and the relaxation mechanism, respectively. In simple cases, the energy distribution function can be inferred from the relaxation behavior. For example, systems with a single activation barrier and relaxation time, as occurring for rare and independent relaxation events, obey the Debye relaxation with $\beta = 1$. More complex relaxation processes as a result of a statistical distribution of relaxation times and many successive correlated activation steps, as persisting in, e.g. supercooled liquids, spin glasses, amorphous solids, molecular systems, glassy soft matter, viscoelastic materials, and granular magnetic films [2–8], can be described by stretched ($0 < \beta < 1$) [9–15] and compressed ($1 < \beta < 3$) [16, 17] exponential functions. Transitions between phases with distinct coordination and short-range order may lead to a crossover from stretched to compressed exponential relaxation [18, 19]. It has proven difficult to rationalize stretched exponential relaxation from the first principles [20] using only a time-independent distribution of activation barriers [12]. In addition, the intermediate range of a stretched exponential

* Author to whom any correspondence should be addressed.

relaxation is logarithmic [21–24] making a classification without knowledge about initial and final relaxation challenging. This contributed to the lack of consensus about its physical origin [12, 13] and inconsistency in literature. Recent proposals pertaining to stretched exponential stress relaxation are based on activation barriers that increase with time [14] due to local relaxation events and their interaction, giving rise to slow stretched-exponential and fast compressed-exponential relaxation [15], or disorder inducing a distribution of local activation barriers [11].

Inhomogeneities have an even stronger influence on the magnetization relaxation. Structural and chemical disorder, magnetic defects, and geometric constraints result in spatial variations in magnetic exchange, anisotropy, and demagnetization fields and cause, by extension, a statistical distribution of activation barriers that profoundly impacts both relaxation mechanism and timescale [25, 26] as a function of temperature and, as we report here, field orientation. For instance, systems consisting of weakly interacting particles reveal a logarithmic (stretched exponential) dependence [21–23] while the magnetization relaxation in homogeneous exchange-coupled materials follows a simple exponential relation [2, 16, 17, 27]. The spontaneous relaxation of the magnetization in materials favoring multi-domain states or of the polarization in relaxor ferroelectrics exhibit a time dependence best described by a power law [28–30]. Another relevant quantity is the exponent γ of the Arrhenius–Néel law [1] for the relaxation time $\tau = \tau_0 \exp[(\frac{\Delta E}{k_B T})^{\gamma}]$ that indicates the leading mechanisms: weak domain wall pinning ($\gamma \approx 1$) [23, 26, 31], uniform switching of single domain particles ($\gamma \approx 2$) [23], or Ising films in the creep regime ($\gamma \approx 0.25$) [32]. The accessibility to the underlying relaxation mechanisms makes magnetic viscosity measurements appealing not only for quantifying the thermal stability of magnetic media, but also for fundamental studies of topological states and phase transitions.

Here, we demonstrate the potential of angle-dependent magnetic viscosity measurements for identifying different magnetization relaxation processes in nanogranular exchange-coupled Co/Pt multilayer stacks with different perpendicular magnetic anisotropy and defect density. The magnitude of the magnetic anisotropy originating from Co–Pt orbital bonding [33] strongly depends on the interface quality which is cleanest for (111) textured films [34, 35]. Varying pressure and deposition power during sputter deposition yields different adatom energies and texturing of the multilayer stack [36]. High adatom energies deteriorate the magnetic anisotropy [37] due to increased interface roughness and intermixing.

2. Structural properties

The [Co(t)/Pt(0.6 nm)]$_5$ multilayers ($t = 0.3, 0.4$ nm) were grown at room temperature by means of magnetron sputtering (2.86×10^{-3} mbar with base pressure 7.7×10^{-8} mbar) on 128° Y-cut lithium niobate substrates (typically used for surface acoustic wave transduction) using a Cr(2 nm)/Pt(2 nm) seed layer and a Pt(1 nm) capping layer. Co and Pt were deposited with DC guns (40 W); Cr was grown using an RF gun (75 W). The thickness of individual cobalt layers together with the Co–Pt orbital hybridization [33] guarantees a sizable perpendicular magnetic anisotropy (see below). The topography of the resulting films was mapped using a Bruker Dimension Icon SPM with Bruker ScanAsyst air tips in tapping mode. Both films possess a nanogranular texture with a root mean square of 0.12 nm for [Co(0.3 nm)/Pt(0.6 nm)]$_5$ averaged over an area of 1 μm^2 and 0.15 nm for [Co(0.4 nm)/Pt(0.6 nm)]$_5$ measured over an area of 0.5 μm^2 (figure 1(a)). The short-range order, size, and shape of individual grains are similar for both samples. The crystalline structure was measured on a Rigaku SmartLab diffractometer equipped with a Cu-K_α radiation source and noise-filtered using a Savitzky–Golay filter with 0.255° window and second-order polynomial (figure 1(b)). The peak positions are identified using the Bragg condition $\theta = 2\arcsin[\lambda/(2d_{hkl})]$ with $\lambda = 0.154$ nm (Cu-K_α) and $d_{khl} = 0.3925/\sqrt{h^2+k^2+l^2}$ nm for cubic platinum and $d_{khl} = 1/\sqrt{4/(3\times 0.5148^2)(h^2+k^2+hk)+l^2/1.3863^2}$ nm for trigonal lithium niobate [38]. The superlattice satellite peaks, recorded on a Bruker D8 Discover diffractometer, are substantially weaker than those reported for multilayer stacks with pure Co/Pt(111) texturing [36] due to interface roughness and intermixing. This effect is enhanced in [Co(0.4 nm)/Pt(0.6 nm)]$_5$ due to longer deposition and larger adatom energy and coincides with an overall lower (111) peak intensity. However, the coexistence of Co/Pt(111) and Co/Pt(110) texturing does neither prevent the emergence of a perpendicular magnetic anisotropy nor exchange-coupling between grains.

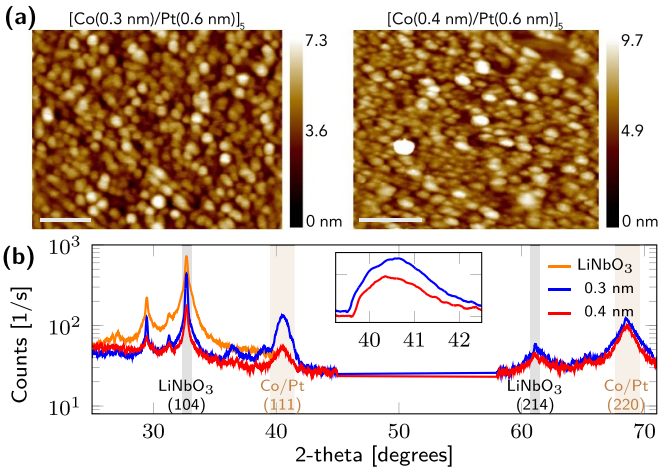

Figure 1. Structural properties of [Co(0.3 nm)/Pt(0.6 nm)]$_5$ and [Co(0.4 nm)/Pt(0.6 nm)]$_5$ films grown on $LiNbO_3$/Cr(2 nm)/Pt(2 nm). (a) Topography measured with atomic force microscopy revealing nanogranular structure. Scale bar is 200 nm. (b) Two-theta x-ray diffraction scans confirming polycrystallinity. The smaller [Co(0.4 nm)/Pt(0.6 nm)]$_5$ film leads to lower counts per second. Inset shows enlarged region of Co/Pt(111) peak with weak superlattice satellite peaks.

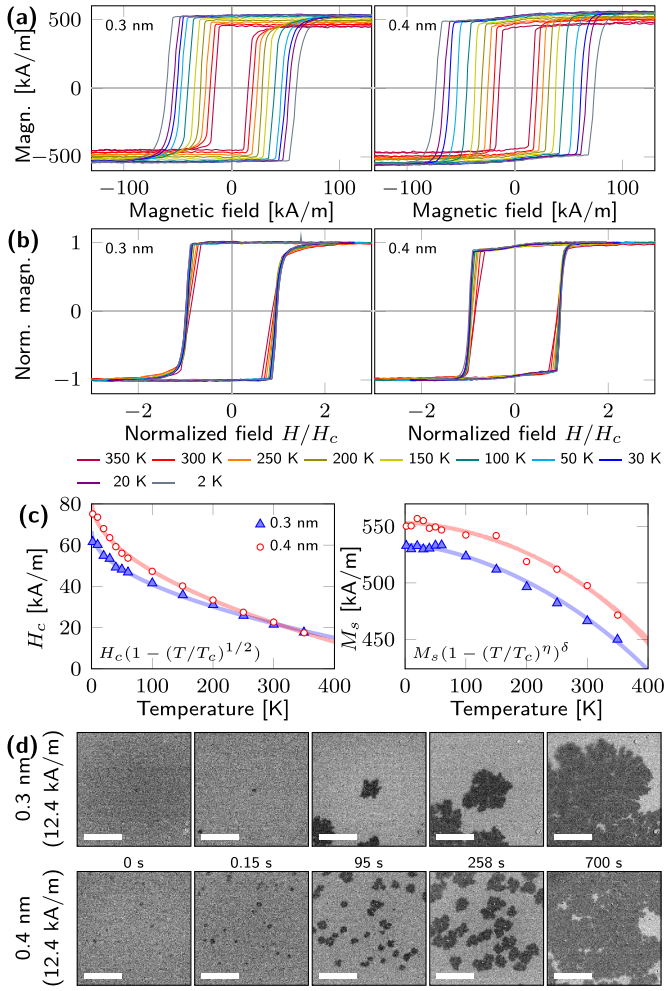

Figure 2. Temperature dependence of magnetic properties of $[Co(0.3\ nm)/Pt(0.6\ nm)]_5$ and $[Co(0.4\ nm)/Pt(0.6\ nm)]_5$ multilayer stacks. (a) Out-of-plane hysteresis loops recorded with vibrating sample magnetometry, (b) collapsed hysteresis loops plotted in (a), and (c) corresponding coercive field and saturation magnetization. (d) Out-of-plane magnetization visualized at room temperature with Kerr microscopy in the presence of a normal bias field highlighting reversal dominated by domain nucleation at defects and domain wall propagation. Scale bar is 50 μm.

3. Temperature dependence of magnetization reversal

The temperature-dependent hysteresis loops of both multilayers, measured with vibrating sample magnetometry with a Quantum Design Physical Properties Measurement System (DynaCool), show evidence of a strong perpendicular magnetic anisotropy, albeit, with slightly slanted flanks (figure 2(a)). Each set collapses into the same normalized hysteresis loop when expressed in units of saturation magnetization M_s and coercive field H_c (figure 2(b)). The slight discrepancy (apparent slope near coercive field) is due to the used field step size of 0.8 kA m^{-1}. Assuming a uniform rotation of the magnetization (Stoner–Wohlfarth), the perpendicular magnetic anisotropy K_u is calculated via $K_u = -\mu_0 \int_{\parallel} M\mathrm{d}H + \mu_0 \int_{\perp} M\mathrm{d}H$ of hysteresis loops taken with H applied in-plane and out-of-plane, respectively. Using all four quadrants implicitly makes, to a great extent, the $M(H)$ data hysteresis-free. In this notation, a positive K_u refers to a perpendicular easy-axis anisotropy. The corresponding room-temperature values for $[Co(0.3\ nm)/Pt(0.6\ nm)]_5$ and $[Co(0.4\ nm)/Pt(0.6\ nm)]_5$ are $K_u = 0.177$ MJ m^{-3} ($K_u = 0.198$ MJ m^{-3}) and $K_u = 0.168$ MJ m^{-3} ($K_u = 0.185$ MJ m^{-3}), respectively, in accordance with literature [36]. Values in parenthesis are retrieved using the in-plane saturation field $H_s \approx 1\ \mathrm{T}/\mu_0$, i.e. $\frac{1}{2}\mu H_s M_s$.

Although the used film thickness and repetition favor uniform, single-domain switching and rectangular shape of the hysteresis, structural defects existing in the film serve as pinning and nucleation sites, which result in a slightly slanted hysteresis (figures 2(a) and (b)), differences between the calculated magnetic anisotropy values, and multi-domain states (figure 2(d)). The latter emerges in the presence of a magnetic bias field due to a domain wall propagation-dominated magnetization reversal (figure 2(d)) mediated by an isotropic dendritic domain expansion [29, 39, 40]. Kerr microscopy [41] further allows for identifying magnetic nucleation sites from the appearance of regions with inverted contrast (switched magnetization) at small magnetic bias fields. This direct inference is necessary since not all structural defects observable in, e.g. atomic force microscopy (figure 1(a)) or electron microscopy act as pinning or nucleation sites for the magnetization. Instead, the nanogranularity might result in spatial variations in magnetic anisotropy and exchange stiffness leading to a distribution of activation barriers. The number of nucleation sites, at a normal bias field 12.4 kA/m, calculated for an area of 44 360 μm^2 is 3 and 60 and equivalent to a structural defect density of $6.8 \times 10^{-5}\ \mu$m^{-2} and $136 \times 10^{-5}\ \mu$m^{-2} for $[Co(0.3\ nm)/Pt(0.6\ nm)]_5$ and $[Co(0.4\ nm)/Pt(0.6\ nm)]_5$, respectively. The increased defect density in $[Co(0.4\ nm)/Pt(0.6\ nm)]_5$ coincides with the overall lesser crystallographic quality (figure 1) and causes earlier initial switching at nucleation sites and delayed saturation at pinning sites. The former are characterized by reduced magnetic exchange and anisotropy yielding a lower activation barrier for magnetization reversal and tilted magnetization in the presence of small magnetic fields. The tilting may even occur at remanence since the perpendicular magnetic anisotropy originating from Co–Pt orbital bonding has to overcome a sizable shape anisotropy favoring an in-plane magnetization. The resulting magnetic hysteresis features a pronounced rectangular shape (switching), a non-vanishing susceptibility near remanence (titled magnetization at nucleation sites invisible to Kerr microscopy), and a prominent tail (multidomain state due to pinning sites) (figures 2(a) and (b)). The tilt-mediated magnetization reversal is corroborated by the angular dependence of the magnetization relaxation (figures 4 and 5) and magnetic coercivity (figure 6).

The temperature dependence of the saturation magnetization can be described by an empirical expression for the spontaneous saturation magnetization $M_s(T) = M_s(0\ \mathrm{K})[1 - (\frac{T}{T_c})^{\eta}]^{\delta}$ (figure 2(c)). Within the investigated temperature range, i.e. at temperatures substantially smaller than the Curie temperature T_c, both empirical expression and data obey the Bloch law [42] for bulk ferromagnets $M_s(T) = M_s(0\ \mathrm{K})[1 -$

$(\frac{T}{2T_c})^{\eta}]$ with an effective transition temperature $\approx 2T_c$. The Curie temperature T_c is estimated from the temperature dependence of the coercive fields (figure 2(c)) to be (667 ± 16) K and (567 ± 14) K for $[\mathrm{Co}(0.3\ \mathrm{nm})/\mathrm{Pt}(0.6\ \mathrm{nm})]_5$ and $[\mathrm{Co}(0.4\ \mathrm{nm})/\mathrm{Pt}(0.6\ \mathrm{nm})]_5$, respectively. These values are in the same ballpark as previously reported [43]. Note that the coercive field coincides only for $[\mathrm{Co}(0.4\ \mathrm{nm})/\mathrm{Pt}(0.6\ \mathrm{nm})]_5$ with the saturation field and is approximately half the saturation field in $[\mathrm{Co}(0.3\ \mathrm{nm})/\mathrm{Pt}(0.6\ \mathrm{nm})]_5$ (figure 2(b)). The critical exponent $\delta = 0.3 \sim 0.4$ agrees with literature values for the analytically exact solution $3/8 = 0.375$ for the 3D Ising model, compared with $1/8$ for the 2D Ising model [44], as well as with Monte Carlo simulations $(0.36 \sim 0.39)$ [45] and experiment $(0.35 \sim 0.4)$ [45–47]. The saturation magnetization normalized to the total volume of Co and Pt is $M_s(0\,\mathrm{K}) = 534\ \mathrm{kA\,m^{-1}}$ and $M_s(0\ \mathrm{K}) = 553\ \mathrm{kA\,m^{-1}}$ for $[\mathrm{Co}(0.3\ \mathrm{nm})/\mathrm{Pt}(0.6\ \mathrm{nm})]_5$ and $[\mathrm{Co}(0.4\ \mathrm{nm})/\mathrm{Pt}(0.6\ \mathrm{nm})]_5$, respectively. Considering an experimental uncertainty of 10%, the saturation magnetization normalized to the Co volume equals the elemental Co magnetic moment retrieved from quantitative x-ray magnetic circular dichroism spectroscopy ($m_{\mathrm{spin}}^{\mathrm{Co}} = 1.6\ \mu_B$ per atom; $m_{\mathrm{orb}}^{\mathrm{Co}} = 0.15\ \mu_B$ per atom [48]) that corroborates an appropriately estimated Co volume. This is because a proximity Pt moment $\lesssim 0.3\ \mu_B$ [49, 50] induced by the Co magnetization at each interface yields an additional relative contribution of $0.3/2.05 < 15\%$. Moreover, both approaches reveal similar η values, namely $1.6 \sim 1.8$ (empirical) and $1.6 \sim 1.7$ (Bloch) in agreement with the nanogranularity of the multilayer stacks, that are slightly elevated from the ideal value $\eta = 1.5$ for homogeneous films [42] observed in, e.g. amorphous materials [51]. The existence of nanocrystals, islands, or defects is known to yield values exceeding 2 [52–54] due to the spatial confinement of thermal spin waves reducing the magnetization at finite temperatures [55]. Another manifestation of the enhanced defect density in $[\mathrm{Co}(0.4\ \mathrm{nm})/\mathrm{Pt}(0.6\ \mathrm{nm})]_5$ is in the larger coercive field and faster decline with temperature (figure 2(c)). Note that the magnetic anisotropy and saturation field are still larger in $[\mathrm{Co}(0.3\ \mathrm{nm})/\mathrm{Pt}(0.6\ \mathrm{nm})]_5$ and that the linear relation between coercive and saturation field (magnetic anisotropy) depends on the homogeneity of the sample, i.e. defect density. In other words, the extracted coercive and saturation fields do not reflect the intrinsic magnetic anisotropy that is expected to be larger in stacks with thinner Co layers.

4. Angular dependence of magnetization relaxation

The angle-dependent relaxation measurements were conducted at room temperature using longitudinal magneto-optical Kerr effect magnetometry (figure 3) [56]. Measurements were taken using a quadrupole electromagnet at field orientations α ranging from 20° to 65° in steps of 5° and skipping 40° and 50° due to experimental constraints. In this notation, 90° refers to the surface normal. The magneto-optical magnetometry setup features a 30 mW 639 nm continuous-wave diode laser and provides a temporal resolution of 20 ms and a spatial resolution <0.5 mm (figure 3). Sensitivity and long-term

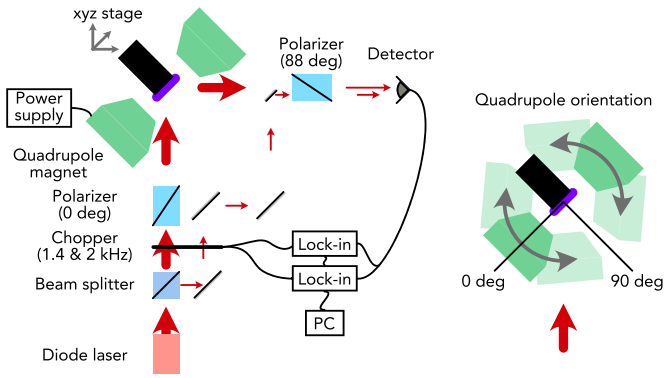

Figure 3. Schematics of optical setup featuring dual-phase lock-in amplification and rotatable quadrupole magnet. The incidence and deflection angle of the light is kept at 45° while the magnetic field angle α can be changed between 20° and 65°. The sample normal is 90°.

stability are guaranteed by modulating the intensity at 1.4 kHz (probe) and 1.68 kHz (reference) with a mechanical chopper and dual-phase lock-in amplification (Stanford Research SR830). Each data point is averaged over a total of 30 periods of the 1.4 kHz signal, i.e. 20 ms. Prior to each magnetic viscosity measurement, hysteresis loops are recorded that exhibit rectangular loops with slight slanted flanks and a magnetic susceptibility that vanishes near remanence (figure 4(a)). Note that this is in stark contrast to the volume-integrated hysteresis loops discussed above (figure 2(a)). The corresponding field range is set to probe the vicinity of the coercive field in steps of $+0.4\ \mathrm{kA\,m^{-1}}$. Even a cursory visual inspection indicates a marked difference between $[\mathrm{Co}(0.3\ \mathrm{nm})/\mathrm{Pt}(0.6\ \mathrm{nm})]_5$ and $[\mathrm{Co}(0.4\ \mathrm{nm})/\mathrm{Pt}(0.6\ \mathrm{nm})]_5$ that becomes more prominent as the field rotates away from normal (figure 4(b)). This sensitivity, particularly in comparison with the magnetic hysteresis loops (figure 4(a)), highlights the strength of angle-dependent magnetization relaxation measurements.

The temporal evolution of the normal magnetization component is mathematically described by a compressed exponential function based on a theory originally developed for crystal growth [57, 58] that accounts for a stochastic nucleation at grains and subsequent expansion. This approximation is well met by the magnetization switching, as evident from Kerr microscopy (figure 2(d)), and yields a remarkably good fit for both samples and all angles (figure 4(b)). In fact, the exponential fits deviate only slightly from experiment for initial and final relaxation in agreement with literature [12]. A relaxation involving N successive correlated relaxation pathways obeys

$$M(t) = -\sum_{i=1}^{N} a_i \exp\left[-\left(\frac{t}{\tau_i}\right)^{\beta_i}\right] + g, \qquad (1)$$

with the relaxation times τ_i, exponents β_i, relative weights a_i, and offset g. For $N \to \infty$, equation (1) becomes the well-known logarithmic dependence [21–23]. Reversal processes where the nuclei do not grow, i.e. uniform switching (Debye relaxation), are described by $\beta = 1$; fast radial expansions of

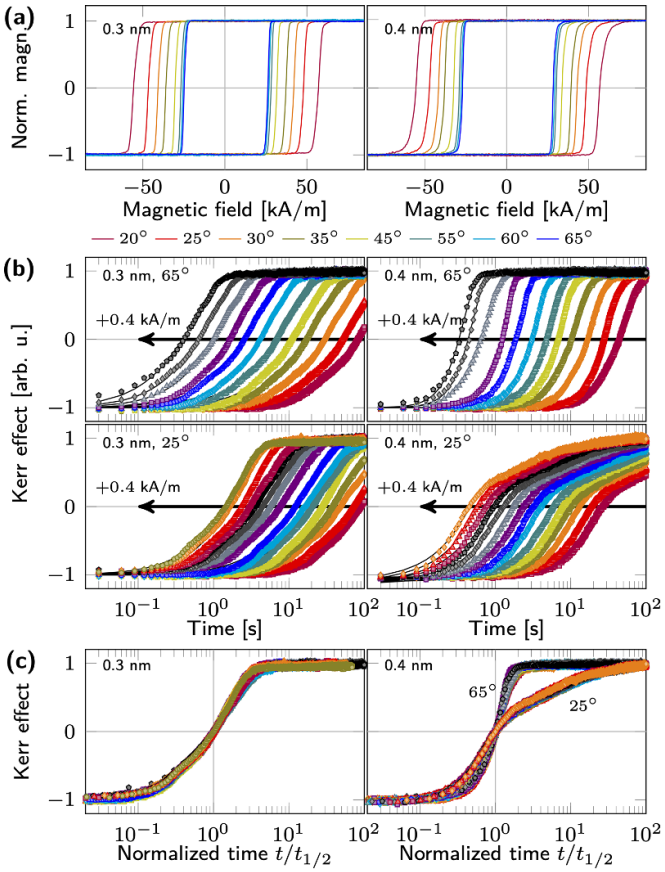

Figure 4. Angular dependence of room-temperature magnetization reversal acquired with magneto-optical magnetometry. (a) Magnetic hysteresis loops for $[Co(0.3\ nm)/Pt(0.6\ nm)]_5$ and $[Co(0.4\ nm)/Pt(0.6\ nm)]_5$ (90° is normal). (b) Magnetization relaxation of (left) $[Co(0.3\ nm)/Pt(0.6\ nm)]_5$ and (right) $[Co(0.4\ nm)/Pt(0.6\ nm)]_5$ in the presence of magnetic bias fields applied at (upper) 65° and (lower) 25° with respect to the sample plane (initially saturated at $-80\ kA\,m^{-1}$). Curves represent bias fields that increase by $+0.4\ kA\,m^{-1}$ from 15.7 (0.3 nm, 65°), 17.9 (0.4 nm, 65°), 31.8 (0.3 nm, 25°), and 34.8 (0.4 nm, 25°) $kA\,m^{-1}$. The single and double exponential functions used to fit the data are described in the text. (c) Collapsed relaxation curves plotted in (b) revealing magnetic field independence and, for $[Co(0.3\ nm)/Pt(0.6\ nm)]_5$, field orientation independence.

the nuclei correspond to $\beta = 3$ [59, 60]. The lower defect density ensures a single pathway ($N = 1$) for the magnetization relaxation in $[Co(0.3\ nm)/Pt(0.6\ nm)]_5$ with small deviations from the single exponential fit upon approaching in-plane geometry (figure 4(b)). These deviations are minor compared with $[Co(0.4\ nm)/Pt(0.6\ nm)]_5$ that requires double exponential fits ($N = 2$) for angles smaller than 65° (figure 4(b)). This profound difference cannot result from the magnetic anisotropy, which differs by only 5% between both systems, but is due to distinct defect densities (20 times). We use $a_{1,2}$, $\tau_{1,2}$, and $\beta_{1,2}$ to refer to the first and second relaxation pathway in $[Co(0.4\ nm)/Pt(0.6\ nm)]_5$ and a, τ, and β without subscript for the single relaxation pathway in $[Co(0.3\ nm)/Pt(0.6\ nm)]_5$.

For each angle, the relaxation curves collapse upon normalization to $t_{1/2}$ (figure 4(c)), which is defined as $M(t_{1/2}) = 0$ and related to the relaxation time τ via $t_{1/2} = [\ln(2)]^{1/\beta}\,\tau$, indicating a field-independent relaxation mechanism (figure 5(a)). The relaxation time is discussed below. There are instances where the shape (β) of the individual curves differs from the rest (figure 4(b)). This process is stochastic since the shape does not reproduce in repeated measurements. With the exception of the second pathway for $[Co(0.4\ nm)/Pt(0.6\ nm)]_5$ (β_2), all cases can be fitted with a compressed exponential function with virtually the same β and β_1 values for a given angle α (figures 5(a) and 6). The field-dependent β_2 value ($0.5 \lesssim \beta_2 \lesssim 1$) is independent of the angle and resembles the trend of the relative weight a_1/a_2 ($1 \lesssim \frac{a_1}{a_2} \lesssim 1.5$) (figure 5(c)). This causes a small opening on either side of the collapsed curves with a slim waist at $t = t_{1/2}$ (figure 4(c)). The ideal case of radial growth of circular domains ($\beta = 3$) is not observed as the domains evolve in a dendritic structure (figure 2(d)). In all cases, the nucleation and domain wall propagation ($\beta \approx 3$) contribution to the relaxation precedes the uniform switching ($\beta \approx 1$). While the β values are similar to those reported in literature for Co/Pt multilayers [61], the observed increase with film thickness is opposite to previous works [27] likely caused by the increased defect density in $[Co(0.4\ nm)/Pt(0.6\ nm)]_5$.

The relaxation times of all three pathways, i.e. τ, τ_1, and τ_2, decrease exponentially with the magnetic field (figure 5(b)) corroborating weak domain wall pinning [23, 26, 31]. This is equivalent to $\gamma = 1$ in the Arrhenius–Néel law for the relaxation time [1]:

$$\tau = \tau_0 \exp\left[\frac{E_0}{k_B T}\left(1 - \frac{H}{H_c}\right)^{\gamma}\right], \qquad (2)$$

with the activation barrier E_0, the coercive field H_c, and the attempt frequency $f_0 = \frac{1}{\tau_0}$ (1 GHz–1 THz). With decreasing angle α, experimental and calculated $t_{1/2}$ (via $t_{1/2} = [\ln(2)]^{1/\beta_1}\,\tau_1$) deviate from each other (figure 5(d)) due to increasing contributions of the second pathway, i.e. underestimated β_1 and $t_{1/2}$, apparent in the collapsed data (figure 4(c)). The transition from a fast compressed to a slow stretched exponential relaxation agrees well with the stress relaxation in inhomogeneous materials where the activation barrier increases in the process of relaxation [14, 15]. This can also be understood from a magnetic perspective where the magnetization relaxation originates from the low-anisotropy nucleation sites with negligible activation barrier followed by an anisotropic domain wall propagation across the inhomogeneous nanogranular film. As the magnetic bias field tilts away from the easy axis (normal direction), it exerts a torque on the magnetization initiating a rather uniform switching via tilting the magnetization ($\beta \to 1$) and an activation barrier E_0 that, according to equation (2) and figure 5(b), decreases with decreasing angle α. This inference is corroborated by the need for the modified Kondorsky model $\frac{H_c(\alpha)}{H_c(90°)} = h + \frac{1-h}{\sin\alpha}$ [62, 63] to describe the angular dependence of the coercive field. The Kondorsky model ($h = 0$) applies to pinning-dominated

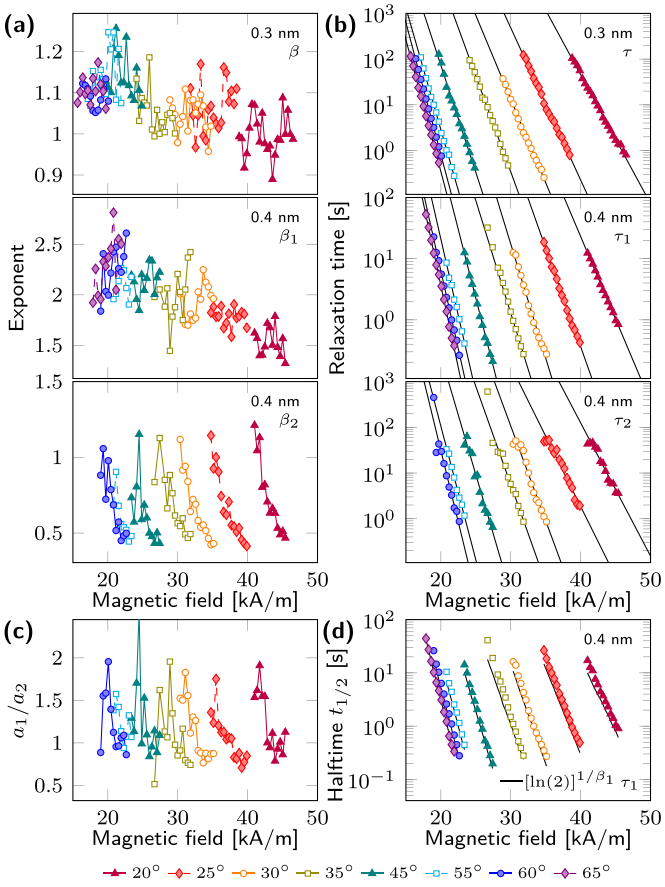

Figure 5. Field and angular dependence of (a) exponents, (b) relaxation times, (c) relative weight of first and second pathway, and (d) halftime extracted from figure 4 (90° is normal). $[Co(0.4\ nm)/Pt(0.6\ nm)]_5$ requires double compressed exponential functions due to the existence of two successive relaxation pathways. Indices 1 and 2 refer to the first and second pathway. The relaxation times are fitted using the Arrhenius–Néel law with $\gamma = 1$. The scatter data in (d) is the experimental data obtained under the condition $M(t_{1/2}) = 0$; the solid lines are calculated using β_1 and τ_1.

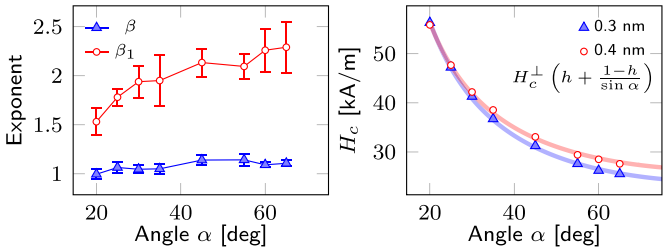

Figure 6. Angular dependence of exponent and coercive field corroborating tilted magnetization vectors due to oblique magnetic bias fields (90° is normal). Coercive fields are fitted using the modified Kondorsky model with $h(0.3\ nm) = 0.29$ and $h(0.4\ nm) = 0.41$.

reversals [64] in systems with large magnetic anisotropy and perfect rectangular hysteresis loops [65] and contrasts coherent rotation of the magnetization (Stoner–Wohlfarth) [66] and incoherent modes, such as curling or buckling [67, 68]. The magnetization reversal in less perfect systems, as discussed here, can be described by the modified Kondorsky model [62, 63] accounting for tilted magnetization vectors during the reversal process [69–71]. The modifications to the simple Kondorsky model are substantial for thicker films, i.e. $h(0.4\ nm) = 0.41$ vs. $h(0.3\ nm) = 0.29$, owing to smaller perpendicular magnetic anisotropy and larger defect density (figure 6).

In conclusion, we synthesized nanogranular Co/Pt multilayers with different perpendicular magnetic anisotropy and defect density to study the angular dependence of the relaxation mechanisms. The critical exponents of the double exponential functions reveal a transition from a pinning-dominated domain wall propagation to a sequence of pinning-dominated and uniform switching, which is corroborated by the scaling of relaxation times and the angular dependence of the coercive field. The torque exerted on the magnetization vector by the oblique magnetic bias field is more efficient in thicker films with increased defect density and smaller perpendicular magnetic anisotropy yielding two successive correlated relaxation pathways with fast compressed and slow stretched exponential relaxation. The enhanced sensitivity of angle-dependent magnetization relaxation measurements to defects may be useful in cases where temperature cannot simply be varied due to constraints by the phase diagram. This includes the unwinding of topological magnetic states in the presence of magnetic, electric, or strain fields and the influence of structural disorder and imperfections.

Data availability statement

All data that support the findings of this study are included within the article (and any supplementary files).

Acknowledgments

This work was supported by the National Science Foundation, Division of Materials Research under Grant No. 2203933. B H and R Z acknowledge support from the University of Nebraska-Lincoln within the Undergraduate Creative Activities & Research Experience program. A A and S A acknowledge funding from the University of Nebraska-Lincoln. This work was in parts performed in the Nebraska Nanoscale Facility and Nebraska Center for Materials and Nanoscience, which are supported by the National Science Foundation under Award No. ECCS: 2025298, and the Nebraska Research Initiative.

ORCID iDs

Anil Adhikari https://orcid.org/0000-0003-4258-6890
Bryce Herrington https://orcid.org/0000-0002-1481-0464
Nhat Nguyen https://orcid.org/0000-0002-1095-1585
Ruthi Zielinski https://orcid.org/0000-0003-3719-0699
Ather Mahmood https://orcid.org/0000-0001-7170-1646

Shireen Adenwalla https://orcid.org/0000-0002-8885-6764
Robert Streubel https://orcid.org/0000-0003-4783-892X

References

[1] Neel L 1949 *Ann. Geophys.* **5** 99
[2] Lottis D K, White R M and Dahlberg E D 1991 *Phys. Rev. Lett.* **67** 362–5
[3] Gotze W and Sjogren L 1992 *Rep. Prog. Phys.* **55** 241–376
[4] Phillips J 1996 *Rep. Prog. Phys.* **59** 1133–207
[5] Sinha G, Chatterjee R, Uehara M and Majumdar A 1996 *J. Magn. Magn. Mater.* **164** 345–56
[6] Angell C A, Ngai K L, McKenna G B, McMillan P F and Martin S W 2000 *J. Appl. Phys.* **88** 3113–57
[7] Gatteschi D and Sessoli R 2003 *Angew. Chem., Int. Ed.* **42** 268–97
[8] Ulrich M, García-Otero J, Rivas J and Bunde A 2003 *Phys. Rev.* B **67** 024416
[9] Kohlrausch R 1847 *Ann. Phys., Lpz.* **12** 393
[10] Chamberlin R V, Mozurkewich G and Orbach R 1984 *Phys. Rev. Lett.* **52** 867–70
[11] Palmer R G, Stein D L, Abrahams E and Anderson P W 1984 *Phys. Rev. Lett.* **53** 958–61
[12] Zwanzig R 1985 *Phys. Rev. Lett.* **54** 364
[13] Phillips J 2006 *J. Non-Cryst. Solids* **352** 4490–4
[14] Trachenko K 2007 *Phys. Rev.* B **75** 212201
[15] Trachenko K and Zaccone A 2021 *J. Phys.: Condens. Matter* **33** 315101
[16] Kirby R D, Shen J X, Hardy R J and Sellmyer D J 1994 *Phys. Rev.* B **49** 10810–3
[17] Nowak U, Heimel J, Kleinefeld T and Weller D 1997 *Phys. Rev.* B **56** 8143–8
[18] Ruta B, Chushkin Y, Monaco G, Cipelletti L, Pineda E, Bruna P, Giordano V M and Gonzalez-Silveira M 2012 *Phys. Rev. Lett.* **109** 165701
[19] Wu Z W, Kob W, Wang W-H and Xu L 2018 *Nat. Commun.* **9** 5334
[20] Dyre J C 2006 *Rev. Mod. Phys.* **78** 953–72
[21] Richter G 1937 *Ann. Phys., Lpz.* **421** 605–35
[22] Street R and Woolley J 1949 *Proc. Phys. Soc.* A **62** 562–72
[23] Gaunt P 1986 *J. Appl. Phys.* **59** 4129
[24] Tsiok O B, Brazhkin V V, Lyapin A G and Khvostantsev L G 1998 *Phys. Rev. Lett.* **80** 999–1002
[25] Flanders P J and Sharrock M P 1987 *J. Appl. Phys.* **62** 2918
[26] Street R and Crew D 1999 *IEEE Trans. Magn.* **35** 4407
[27] Xi H, Gao K Z, Ouyang J, Shi Y and Yang Y 2008 *J. Phys.: Condens. Matter* **20** 295220
[28] Viehland D, Li J F, Jang S J, Cross L E and Wuttig M 1992 *Phys. Rev.* B **46** 8013–7
[29] Sampaio L C, Albuquerque M and Menezes F 1996 *Phys. Rev.* B **54** 6465–72
[30] Adamchuk D, Grigalaitis R, Svirskas S, Macutkevic J, Palaimiene E, Banys J, Mitoseriu L, Canu G, Buscaglia M T and Buscaglia V 2019 *Ferroelectrics* **553** 103–10
[31] Gaunt P 1983 *Phil. Mag.* B **48** 261–76
[32] Lemerle S, Ferré J, Chappert C, Mathet V, Giamarchi T and Le Doussal P 1998 *Phys. Rev. Lett.* **80** 849–52
[33] Nakajima N, Koide T, Shidara T, Miyauchi H, Fukutani H, Fujimori A, Iio K, Katayama T, Nývlt M and Suzuki Y 1998 *Phys. Rev. Lett.* **81** 5229–32
[34] Parkin S S P, Farrow R F C, Marks R F, Cebollada A, Harp G R and Savoy R J 1994 *Phys. Rev. Lett.* **72** 3718
[35] Johnson M T, Bloemen P J H, den Broeder F J A and de Vries J J 1996 *Rep. Prog. Phys.* **59** 1409
[36] Yıldırım O, Marioni M A, Falub C V, Rohrmann H, Jaeger D, Rechsteiner M, Schneider D and Hug H J 2022 *Scr. Mater.* **207** 114285
[37] Carcia P F, Shah S I and Zeper W B 1990 *Appl. Phys. Lett.* **56** 2345
[38] Iyevlev V, Kostyuchenko A, Sumets M and Vakhtel V 2011 *J. Mater. Sci., Mater. Electron.* **22** 1258
[39] Woodward R C, Lance A M, Street R and Stamps R L 2003 *J. Appl. Phys.* **93** 6567–71
[40] Jagla E A 2005 *Phys. Rev.* B **72** 094406
[41] Pommier J, Meyer P, Pénissard G, Ferré J, Bruno P and Renard D 1990 *Phys. Rev. Lett.* **65** 2054–7
[42] Bloch F 1930 *Z. Phys.* **61** 206
[43] Lin C-J, Gorman G, Lee C, Farrow R, Marinero E, Do H, Notarys H and Chien C 1991 *J. Magn. Magn. Mater.* **93** 194–206
[44] Zhang Z-D 2007 *Phil. Mag.* **87** 5309–419
[45] Pelissetto A and Vicari E 2002 *Phys. Rep.* **368** 549–727
[46] Seeger M, Kaul S N, Kronmüller H and Reisser R 1995 *Phys. Rev.* B **51** 12585–94
[47] Chikazumi S 2009 *Physics of Ferromagnetism* (*International Series of Monographs on Physics*) (Oxford University Press)
[48] Chen C T, Idzerda Y U, Lin H-J, Smith N V, Meigs G, Chaban E, Ho G H, Pellegrin E and Sette F 1995 *Phys. Rev. Lett.* **75** 152
[49] Geissler J, Goering E, Justen M, Weigand F, Schütz G, Langer J, Schmitz D, Maletta H and Mattheis R 2001 *Phys. Rev.* B **65** 020405
[50] Yang H, Thiaville A, Rohart S, Fert A and Chshiev M 2015 *Phys. Rev. Lett.* **115** 267210
[51] Streubel R *et al* 2021 *Adv. Mater.* **33** 2004830
[52] Senz V, Röhlsberger R, Bansmann J, Leupold O and Meiwes-Broer K-H 2003 *New J. Phys.* **5** 47
[53] Maaz K, Mumtaz A, Hasanain S K and Bertino M F 2010 *J. Magn. Magn. Mater.* **322** 2199
[54] Obaidat I M, Nayek C and Manna K 2017 *Appl. Sci.* **7** 1269
[55] Hendriksen P V, Linderoth S and Lindgård P-A 1993 *Phys. Rev.* B **48** 7259
[56] Kerr J 1877 *London, Edinburgh Dublin Phil. Mag. J. Sci.* **3** 321
[57] Kolmogorov A N 1937 *Bull. Acad. Sci. USSR, Math. Ser.* **1** 355–9
[58] Avrami M 1940 *J. Chem. Phys.* **8** 212–24
[59] Fatuzzo E 1962 *Phys. Rev.* **127** 1999–2005
[60] Labrune M, Andrieu S, Rio F and Bernstein P 1989 *J. Magn. Magn. Mater.* **80** 211–8
[61] Choe S-B and Shin S-C 1998 *Phys. Rev.* B **57** 1085–9
[62] Schumacher F 1991 *J. Appl. Phys.* **70** 3184
[63] Lee T Y and Huang H L 1993 *J. Appl. Phys.* **74** 495
[64] Kondorsky E 1940 *J. Phys.* **II** 161–81
[65] Reich S, Shtrikman S and Treves D 1965 *J. Appl. Phys.* **36** 140–1
[66] Stoner E C and Wohlfarth E P 1948 *Phil. Trans. R. Soc.* A **240** 599
[67] Aharoni A and Shtrikman S 1958 *Phys. Rev.* **109** 1522–8
[68] Ferré R, Ounadjela K, George J M, Piraux L and Dubois S 1997 *Phys. Rev.* B **56** 14066–75
[69] Ghidini M, Zangari G, Prejbeanu I L, Pattanaik G, Buda-Prejbeanu L D, Asti G, Pernechele C and Solzi M 2006 *J. Appl. Phys.* **100** 103911
[70] Streubel R, Thurmer D J, Makarov D, Kronast F, Kosub T, Kravchuk V, Sheka D D, Gaididei Y, Schäfer R and Schmidt O G 2012 *Nano Lett.* **12** 3961–6
[71] Puwenberg N, Reiche C F, Streubel R, Khan M, Mukherjee D, Soldatov I V, Melzer M, Schmidt O G, Büchner B and Mühl T 2019 *Phys. Rev.* B **99** 094438